An analytical solution for the undrained horizontal-torsional resistance of mudmats

X. Feng[1], M. F. Randolph[1] and S. Gourvenec[1]

[1]Xiaowei FENG
Centre for Offshore Foundation Systems – M053
A node of the ARC Centre of Excellence for Geotechnical Science and Engineering
University of Western Australia
35 Stirling Highway, Crawley
Perth, WA 6009
Australia
Tel: +61 8 6488 2473
Fax: +61 8 6488 1044
Email: xiaowei.feng@uwa.edu.au

[1]Mark F. RANDOLPH
Centre for Offshore Foundation Systems
A node of the ARC Centre of Excellence for Geotechnical Science and Engineering
University of Western Australia
Tel: +61 8 6488 3075
Email: mark.randolph@uwa.edu.au

[1]Susan GOURVENEC
Centre for Offshore Foundation Systems
A node of the ARC Centre of Excellence for Geotechnical Science and Engineering
University of Western Australia
Tel: +61 8 6488 3995
Email: susan.gourvenec@uwa.edu.au

No. of words: 4261 (without abstract and references)
No. of tables: 4
No. of figures: 20

44 **An analytical solution for the undrained horizontal-torsional resistance of**

45 **mudmats**

46 X. Feng[1], M.F. Randolph[1] and S. Gourvenec[1]

47 **ABSTRACT**

48 Rectangular mudmat foundations are frequently used for supporting subsea structures for

49 offshore oil and gas developments. The self-weight of the subsea structure and mudmat often

50 mobilise a relatively small proportion of the vertical bearing capacity and horizontal-torsional

51 sliding generally represents the governing load case. However, the effect of torsion on mudmat

52 capacity is not explicitly considered in current guidelines for geotechnical design of offshore

53 foundations. In this paper, upper bound plastic limit analysis is used to develop explicit

54 expressions for the combined horizontal and torsional capacity of skirted mudmats. The results

55 of the limit analyses are compared with results from finite element analysis, and with other

56 published solutions. A method is proposed for estimating the translational sliding resistance

57 from the interaction diagram for biaxial horizontal loading and a unique expression is proposed

58 to define the normalised H-T failure envelope. The effect of foundation aspect ratio, foundation

59 embedment ratio, skirt-soil interface roughness, direction of horizontal loading and degree of

60 soil strength heterogeneity are investigated systematically.

61 **KEYWORDS**

63

---

[1] Centre for Offshore Foundation Systems, The University of Western Australia

64 **INTRODUCTION**

65 Mudmat foundations are employed extensively to support subsea infrastructure, such as

66 manifolds, pipeline end terminations and in line structures. Mudmat foundations for subsea

67 infrastructure are typically square or rectangular in plan and consist of a top cap and an

68 arrangement of peripheral and internal skirts. The external loads transmitted to subsea mudmats

69 are often in six degrees-of-freedom. In addition to the self-weight of the foundation and

70 supported structure, thermal expansion and contraction of the pipelines and jumpers, which

71 connect to the foundations at vertical and bi-axial horizontal eccentricity, lead to significant

72 horizontal load (H), moment (M) and torsion (T). The vertical load mobilisation is generally

73 small, and the dominant loads are typically the resultant H (acting at an angle to the foundation

74 sides) and the induced torsion. This contrasts with platform foundations, where higher vertical

75 load mobilisation acts in combination with horizontal load and overturning moment. Even

76 though horizontal-torsional sliding may often represent the governing load case in practice, the

77 detrimental effect of torsion on the horizontal capacity is not explicitly described in current

78 offshore guidelines for shallow foundations (e.g. API, 2011; ISO, 2003). The effect of torsion

79 on horizontal capacity was considered by Finnie and Morgan (2004) on the basis of an

80 artificially reduced strength at foundation sliding level. More recently, a 'failure envelope'

81 approach was used to assess the combined H-T loading capacity of subsea foundations

82 considering intact contact between the external skirt walls and the soil (e.g. Murff et al., 2010;

83 Nouri et al., 2014). A general ellipse for describing the H-T failure envelopes was proposed by

84 Nouri et al. (2014), but the exponents were not explicitly defined as a function of foundation

85 and soil conditions. Furthermore, a 'gap' along the vertical skirt-soil interface, with water being

86 sucked in once the normal effective stress reduces to zero, may be initiated by the significant

87 torsion, horizontal load, overturning moment, or scour, which may jeopardise foundation

88 capacity (Acosta-Martinez et al., 2010; Mana et al., 2013).

89 In this paper, the horizontal-torsional capacity of mudmat foundations is investigated by upper

90 bound plastic limit analysis (PLA) and finite element analysis (FEA). The advances of the

91 current work over previous published work (Murff el al. 2010; Nouri et al., 2014) are the

92 proposed general expressions that fully define the failure envelopes for translational sliding and

93 torsional sliding and quantify the complex effects of foundation aspect ratio and embedment

94 ratio, skirt roughness, direction of horizontal loading, soil strength heterogeneity and gapping

95 adjacent to the mudmat skirts. The expressions developed enable initial design calculations for

96 subsea mudmats subjected to any combination of coplanar translation and torsion, avoiding ad

97 hoc PLA to define the interaction diagrams for a specific project.

98 **BOUNDARY VALUE PROBLEM**

99 The boundary value problem considered in this study is undrained failure of a rectangular

100 mudmat with width-to-length ratios B/L of 0.5, 0.75 and 1, and skirt embedment ratios of d/B

101 = 0.05, 0.1 and 0.2. The shear strength of the soil was modelled as either uniform with depth or

102 increasing linearly with depth according to $s_u = kz$, where k is the shear strength gradient with

103 depth, z. For this particular problem, the critical shear strengths are those at skirt tip level, s_{u0},

104 and the average value over the depth of the skirts, $s_{u,avg}$. The shear strength profiles considered

105 cover a range for $s_{u,avg}/s_{u0}$ of 0.5 to 1. Full skirt-soil contact and gapping along the active edges

106 of the foundation skirt are considered.

107 **PLASTIC LIMIT ANALYSIS**

108 Upper bound plastic limit analysis was carried out to provide estimates of the horizontal-

109 torsional resistance independently from the results of FEA. The approach requires a

110 kinematically admissible mechanism for which work done by external forces is equated to the

111 internal plastic work. The unknown force is evaluated and subsequently minimized with respect

112 to parameters defining the mechanism geometry.

113 **Soil failure mechanisms**

114 The kinematically admissible mechanism for purely translational sliding under biaxial

115 horizontal loading, or H_x-H_y loading, is shown in Figure 1, including shear failure across the

116 foundation base, passive bearing failure of soil against the leading edges (wedges indicated by

117 solid lines) and active bearing failure of soil against the trailing edges, if activated (wedges

118 indicated by dashed lines). The form of the deformation mechanism is an extension of that used

119 for strip foundations (Bransby & Randolph, 1999). The kinematic mechanism under H-T

120 loading is built on that proposed by Murff et al. (2010), but with a gap allowed along the active

121 (trailing) edge skirts. The distributions of passive and active failure vary with the location of

122 the rotation centre, (x_c, y_c) with a general failure mechanism shown in Figure 2 where the centre

123 of rotation falls within the foundation footprint. If the rotation centre falls outside the footprint,

124 passive or active wedges may run along the entire length of particular sides. The difference

125 from translational sliding is that the shear failure is torsional and the soil wedges are continually

126 deforming regions. The horizontal displacement, u will vary along the wedges (shown in Figure

127 1), resulting in internal shear.

128   **Gapping**

129   Geometrically similar wedges are assumed to form along the passive and active zones of an

130   embedded foundation in soil with sufficiently low shear strength ratio $s_{u,avg}/\gamma'd$, where γ' is the

131   effective unit weight of the soil, and d is the skirt depth. For shear strength ratios above a critical

132   value, a gap may develop with detachment of the skirt from the soil in the active zones. In this

133   case, the mechanism will involve only the passive wedges. The upper bound estimate of the

134   shear strength ratio necessary for stability of an unsupported plane strain soil wedge is

$$\frac{s_{u,avg}}{\gamma'd} \geq 0.25 \tag{1}$$

135   with $s_{u,avg}$ being the undrained shear strength at skirt mid-depth. This is within 6% of the best

136   'exact' plane strain solution of 0.27 (Martin, 2011). The stability ratio for plane strain compares

137   with that for unsupported axisymmetric excavations in soft clay of 0.25 and 0.18, for excavation

138   depth to diameter ratios of 0.1 and 0.5 (Britto & Kusakabe, 1982). A gap is unlikely to be

139   initiated in a deposit with a shear strength ratio less than this value since the soil strength will

140   be insufficient to support the exposed face of the gap.

141   **FINITE ELEMENT ANALYSIS**

142   **Geometry and soil model**

143   The ABAQUS 6.11 finite element package was used for all analyses.

144   The soil was modelled as linear elastic, perfectly plastic obeying a Tresca failure criterion. The

145   elastic properties were defined by undrained Young's modulus $E = 1000s_u$ and Poisson's ratio

146   of $v = 0.49$ (i.e. almost incompressible). The meshes extended 3B from the edges of the

147   foundation and 3B beneath the level of pile skirt tips, with horizontally constrained nodes at the

148   sides, and fully constrained nodes at the base. A half view of the fully three-dimensional FE

149   mesh is shown in Figure 3 for the case of d/B = 0.1, B/L = 0.5. The full mesh comprised 82,100

150   8-node, brick hybrid elements, with a particularly thin layer of elements ($\approx 0.3\%$B thick)

151   immediately beneath the foundation base level and concentrated in the region of soil adjacent

152   to the foundation edge ($\approx 0.4\%$B thick) to assist with translational and torsional sliding

153   mechanisms.

154   The mudmat was modelled as a perfect rigid body, with the load reference point taken as the

155   centroid of the top cap, which aligns with the mudline. The underside of the mudmat was fully

156 bonded with the subsoil. Two different interfaces between the side surface of the mudmat and

157 the soil were considered (i) rough side (R) with no separation from the soil, i.e. fully bonded;

158 (ii) smooth side (S) allowing for detachment from the soil, i.e. enabling initiation of, but not

159 prescribing, a gap behind the trailing (active) skirts.

Probing failure envelopes

160

161 This study focuses on failure envelopes arising from interaction of the horizontal and torsional

162 loading in the absence of other loads. The mudmat is permitted to translate in the vertical

163 direction and rotate about a horizontal axis (i.e. in a vertical plane) while the probe tests are

164 being performed in the FEA. Load-controlled fixed-ratio probe tests with different

165 combinations of horizontal load and torsion were mainly employed to detect the failure

166 envelopes, offering straightforward comparison with results of PLA. The loading path from a

167 load-controlled probe terminates when it reaches the H-T failure envelope, indicated by failing

168 the convergence check. Very small load increments are necessary for a load-controlled probe

169 as failure is approached in order not to overshoot the failure envelope. Displacement-controlled

170 fixed-ratio probes tests were also adopted, providing independent checks of the failure

171 envelopes obtained from load-controlled probe tests.

172 **RESULTS**

173 **Pure horizontal capacity**

174 Under pure horizontal load parallel to one of the sides, the direction of motion of mudmat

175 sliding θ_u is identical with that of the load, θ. Only soil wedges along the long sides of the

176 mudmat normal to the horizontal load are activated. The plastic work on the displacement

177 discontinuities and due to potential energy changes can be determined from Table 1 and

178 equation (8) (presented later) by substituting $\theta_u = 0$ for H applied parallel to the short side of

179 the foundation, B, or $\theta_u = \pi/2$ for H applied parallel to the long side of the foundation, L. By

180 equating the external work input to the internal work, the ultimate horizontal loads can be

181 expressed as:

$$\frac{H_{xult}}{As_{u0}} = 1 + N_{px}\frac{d}{B} \tag{2a}$$

$$\frac{H_{yult}}{As_{u0}} = 1 + N_{py}\frac{d}{L} \tag{2b}$$

182   Where

$$N_{px} = \left(\frac{\delta}{\sin\beta\cos\beta} + \delta\alpha_{skirt}\left(\tan\beta + \frac{B}{L}\right) + (2-\delta)\frac{\gamma'd}{2s_{u,avg}} \right)\frac{s_{u,avg}}{s_{u0}} + \frac{\delta}{3\sin\beta}\frac{d}{L}\left(\frac{4s_{u,avg}}{s_{u0}} - 1\right) \quad (3a)$$

$$N_{py} = \left(\frac{\delta}{\sin\beta\cos\beta} + \delta\alpha_{skirt}\left(\tan\beta + \frac{L}{B}\right) + (2-\delta)\frac{\gamma'd}{2s_{u,avg}} \right)\frac{s_{u,avg}}{s_{u0}} + \frac{\delta}{3\sin\beta}\frac{d}{B}\left(\frac{4s_{u,avg}}{s_{u0}} - 1\right) \quad (3b)$$

183   where α_{skirt} = skirt friction ratio, i.e. the ratio of the limiting shear stress along the skirts to the

184   soil undrained shear strength, $\delta = 1$ or 2 for a one- or two-sided mechanism respectively. In

185   general, one-sided mechanism pertains to formation of gaps and two-sided to absence of

186   gapping. For an infinitely long strip foundation, i.e. B/L = 0, the equation simplifies to the

187   solution given by Bransby & Randolph (1999).

188   For a smooth rectangular foundation ($\alpha_{skirt} = 0$) embedded in uniform soil ($s_{u,avg}/s_{u0} = 1$) and

189   allowing for gaps ($\delta = 1$), equation (3) reduces to

$$N_{px} = \frac{1}{\sin\beta\cos\beta} + \frac{1}{\sin\beta}\frac{d}{L} + \frac{\gamma'd}{2s_{u,avg}} \quad (4a)$$

$$N_{py} = \frac{1}{\sin\beta\cos\beta} + \frac{1}{\sin\beta}\frac{d}{B} + \frac{\gamma'd}{2s_{u,avg}} \quad (4b)$$

190   For a rough rectangular foundation ($\alpha_{skirt} = 1$) embedded in normally consolidated soil ($s_{u,avg}/s_{u0}$

191   = 0.5), assuming a two-sided failure mechanism is applicable ($\delta = 2$), and equation (3) reduces

192   to

$$N_{px} = \frac{1}{\sin\beta\cos\beta} + \tan\beta + \frac{B}{L} + \frac{2}{3\sin\beta}\frac{d}{L} \quad (5a)$$

$$N_{py} = \frac{1}{\sin\beta\cos\beta} + \tan\beta + \frac{L}{B} + \frac{2}{3\sin\beta}\frac{d}{B} \quad (5b)$$

193   The values of β for the optimised solutions are summarised in Table 2 for a rectangular (B/L =

194   0.5) and square foundations under the corresponding boundary conditions specified in

195   equations (4) and (5). Given that the value of β is practically 45° for the $\alpha_{skirt} = 0$, $s_{u,avg}/s_{u0} = 1$

196   case and 35° for the $\alpha_{skirt} = 1$, $s_{u,avg}/s_{u0} = 0.5$ case for all aspect ratios, equation (4) yields

$$N_{px} = 2 + 1.41\frac{d}{L} + \frac{\gamma' d}{2s_{u,avg}} \tag{6a}$$

$$N_{py} = 2 + 1.41\frac{d}{B} + \frac{\gamma' d}{2s_{u,avg}} \tag{6b}$$

197　　and equation (5) gives

$$N_{px} = 2.83 + \frac{B}{L} + 1.16\frac{d}{L} \tag{7a}$$

$$N_{py} = 2.83 + \frac{L}{B} + 1.16\frac{d}{B} \tag{7b}$$

198　　For an embedded foundation, the horizontal capacity consists of base shearing resistance and
199　　the additional resistance provided by the peripheral skirts, as indicated by equation (2). The
200　　horizontal capacities along the x- and y-axis derived by PLA for foundations with B/L of 0.5
201　　are presented in Figure 4 together with the results of FEA for the prescribed conditions adopted
202　　for equations (4) and (5). The base shearing resistance derived from the FEA was approximately
203　　5% higher than the theoretical solution of unity due to shearing across the finite thickness layer
204　　of elements beneath the foundation in the FEA rather than shearing across an infinitesimally
205　　thin plane in the PLA. However, the discrepancy in overall resistance reduces as the skirt depth
206　　increases, due to slight over prediction using PLA of the resistances in the wedges.

207　　**Pure torsional capacity**

208　　The failure mechanism under pure torsion is as shown in Figure 2, with the rotation centre
209　　located at the origin, i.e. $x_c = y_c = 0$. For an optimised solution, the failure mechanism needs to
210　　be symmetrical, i.e. $\beta_1 = \beta_3$ and $\beta_2 = \beta_4$, where β_1, β_2, β_3 and β_4 are the slope angles of the soil
211　　wedges. The torsional solutions derived by PLA for foundations with B/L of 0.5 are presented
212　　in Figure 5 together with the results of FEA for the same boundary conditions considered for
213　　calculating the horizontal capacities (shown in Figure 3). The torsional base shearing resistance
214　　obtained from FEA is 8% higher than the theoretical solution derived by Murff et al. (2010) for
215　　a surface foundation ($t_0 = T_{ult}/ALs_{u0} \approx 0.30$), again due to shearing across a finite thickness
216　　layer at tip level.

Translational sliding under combined biaxial horizontal load

The resultant horizontal load transmitted to subsea mudmats from attached pipelines and jumpers acts at an angle from the short or the long side of the foundation. The horizontal capacity in a given loading direction can be determined from failure envelopes in the H_x-H_y loading plane. For a given angle of resultant horizontal load, $\theta = \tan^{-1}(H_y/H_x)$, the kinematic mechanism shown in Figure 1, with associated plastic work, was used to give a prediction of the unknown load. Thus for H_x the work equation is

$$H_x\left(\cos\theta_u + \tan\theta \cdot \sin\theta_u\right)u = \sum \Delta W - \Delta W_{\gamma H} \tag{8}$$

where $\Sigma\Delta W =$ the total plastic work on the displacement discontinuities. $W_{\gamma H}$ is the work done by the self-weight of soil, given by

$$\Delta W_{\gamma H} = (\delta - 2)\frac{\gamma' d^2}{2}\left(L\cos\theta_u + B\sin\theta_u\right)u \tag{9}$$

The plastic work contributions ΔW on the displacement discontinuities are summarised in Table 1. The minimum upper bound value of the unknown load was obtained by optimising the variables β_1, β_2 and θ_u. The two-sided failure mechanism should be symmetrical giving $\beta_3 = \beta_1$ and $\beta_4 = \beta_2$. The H_x-H_y failure envelopes derived from the PLA are compared to those from the FEA in Figure 6. The contours of the equivalent plastic strain obtained from FEA presented in Figure 7a and b correspond to the points A and B in Figure 6 for the cases when the horizontal load is applied in the direction of $\theta = 45°$, and show the one- and two-sided soil failure mechanisms adjacent to the mudmats, reflecting the assumed mechanisms in Figure 1 for the PLA. The PLA and FEA solutions generally agree well; the PLA results fall slightly under the FEA results with the difference mainly arising from the over-prediction of the mobilised base shear resistance due to shearing in a finite thickness layer of elements in the FEA (as described above for pure horizontal sliding capacity).

For a surface foundation, the optimised horizontal capacity is achieved when the direction of motion of foundation sliding is identical to that of the horizontal load, $\theta_u = \theta$. Ultimately, a circle is obtained to represent the failure envelope, expressed as

$$\left(\frac{H_x}{As_{u0}}\right)^2 + \left(\frac{H_y}{As_{u0}}\right)^2 = 1 \tag{10}$$

241   This reflects the basal sliding resistance of an embedded foundation being equal to the product

242   of base area and soil shear strength at foundation level, irrespective of the loading direction.

243   Figure 8 shows the failure load for a given direction of motion of slide for embedded

244   foundations. By assuming a direction of motion θ_u, the two components of the failure load can

245   be expressed as

$$H_x = As_{u0}\cos\theta_u + \Delta H_x \tag{11a}$$

$$H_y = As_{u0}\sin\theta_u + \Delta H_y \tag{11b}$$

246   where ΔH_x and ΔH_y are the additional capacity provided by the skirts along the short side and

247   long side of the foundation, respectively. Therefore, the failure envelopes for basal sliding of

248   the embedded foundations can be expressed as

$$\left(\frac{H_x - \Delta H_x}{As_{u0}}\right)^2 + \left(\frac{H_y - \Delta H_y}{As_{u0}}\right)^2 = 1 \tag{12}$$

249   The H_x-H_y failure envelopes can then be determined after the interaction diagram for ΔH_x-ΔH_y

250   loading is established for given direction of motion θ_u. For foundations with smooth skirts, the

251   interaction between the components of the additional capacity provided along the short side and

252   long side of the foundation is insignificant and independent of the direction of motion θ_u (Figure

253   9a), i.e. $\Delta H_x = \Delta H_{xult} = N_{px}dLs_{u0}$, $\Delta H_y = \Delta H_{yult} = N_{py}dBs_{u0}$, where ΔH_{xult} and ΔH_{yult} are the

254   ultimate additional capacities along the x- and y-axes, which can be determined

255   straightforwardly using the skirt bearing capacity factor given by equation (3). Therefore, the

256   value of θ' (see Figure 8) is determined as

$$\theta' = \tan^{-1}(\Delta H_y/\Delta H_x) = \tan^{-1}(N_{py}B/N_{px}L) \tag{13}$$

257   The corresponding H_x-H_y failure envelope can then be determined straightforwardly by using

258   equations (3) and (10). The interaction becomes more evident for the case of rough skirts

259   (Figure 9b) because of the resistance contribution induced by the interface shearing between

260   the skirt and adjacent soil. However, the failure loads on the normalised ΔH_x-ΔH_y plot for the

261   case of rough skirts were found to be independent of the foundation embedment and soil

262   strength heterogeneity, as shown in Figure 10. A unique elliptical expression was proposed for

263   predicting the interaction between the two components of the additional capacity provided by

264   the skirts.

$$\left(\frac{\Delta h_x - \xi}{1 - \xi}\right)^{2.3} + \left(\frac{\Delta h_y - (1 - \xi)}{\xi}\right)^{2.3} = 1 \quad (\xi \le \Delta h_x \le 1; 1 - \xi \le \Delta h_y \le 1) \tag{14}$$

265   where Δh_x and Δh_y are the normalised additional capacity, defined respectively as $\Delta h_x =$
266   $\Delta H_x / \Delta H_{xult}$ and $\Delta h_y = \Delta H_y / \Delta H_{yult}$. The effect of the aspect ratio, B/L, typically 0.5 to unity in
267   field conditions, on the shape of the normalised ΔH_x-ΔH_y failure envelopes is considered by a
268   parameter ξ, given by

$$\xi = 0.7 - 0.2\frac{B}{L} \tag{15}$$

269   The H_x-H_y failure envelopes for embedded foundations consist of three zones as shown in
270   Figure 11. Zone 2 corresponds to the soil failure mechanism presented in Figure 1 and
271   dominates the whole failure envelope. The very small segments of Zone 1and Zone 3 indicate
272   that the foundation translates along x- and y-axis, respectively. The parameter ξ defines the
273   position of transition of soil failure mechanisms from Zone 1 to Zone 2 then Zone 3 as the
274   direction of horizontal load θ increases from 0° to 90°.

275   The additional capacity of ΔH_x and ΔH_y can then be solved on the ΔH_x-ΔH_y plot for a given
276   angle θ', which is a function of the direction of sliding θ_u and foundation aspect ratio B/L (Figure
277   12), expressed as

$$\theta' = 0.36\left(\theta_u + \frac{B}{L}\right) + 0.15 \tag{16}$$

278   The intercepts at the vertical axes on the plots shown in Figure 12 are the values of θ' at the
279   transition of failure mechanisms from Zone 1 to Zone 2.

280   To this stage, the general ellipse of the H_x-H_y failure envelopes for embedded mudmat
281   foundations can be established following the procedure presented in Table 3 based on the
282   interaction diagram in Figure 8. For practical use, the shape of H_x-H_y failure envelopes can be
283   explicitly described by

$$\left(\frac{H_x}{H_{xult}}\right)^q + \left(\frac{H_y}{H_{yult}}\right)^r = 1 \tag{17}$$

284   The shape of failure envelope is insensitive to the foundation aspect ratio and skirt roughness.
285   The exponents of q and r can be determined by

11

$$q = 2 + 2\left(4\frac{s_{u,avg}}{s_{u0}} - 1\right)\frac{d}{B} \tag{18a}$$

$$r = 2 + 6\frac{d}{B} \tag{18b}$$

286   The quality of the curve fitting is shown in Figure 13 and Figure 14 for mudmats with rough

287   skirts and smooth skirts, respectively.

Torsional sliding under combined horizontal-torsional load

289   For a prescribed loading path, $T/H = e$, in the H-T loading plane, the kinematic mechanism

290   (Figure 2) with associated plastic work was used to give a prediction of the unknown load, e.g.

291   H, at failure by optimising the unknown variables x_c, y_c, β_1, β_2, β_3 and β_4.

292   The work equation is

$$H\cos\theta \cdot y_c\omega + H\sin\theta \cdot x_c\omega + T \cdot \omega = \sum \Delta W - \Delta W_{\gamma T} \tag{19}$$

293   where $\Sigma\Delta W$ = total plastic work, as documented in Table 4. The integration limits and the

294   distribution of activated active and passive soil wedges vary for different locations of the

295   rotation centre, and for different prescribed conditions. $W_{\gamma T}$ is the work done by the self-weight

296   of soil wedges, given by (see derivation in Appendix A):

$$\Delta W_{\gamma T} = (\delta - 2)\frac{\gamma' d^2}{16}\left(\begin{array}{l}\text{Min}(L + 2y_c, 2L)\text{Max}(L + 2y_c, 4y_c) + \text{Min}(B + 2x_c, 2B)\text{Max}(B + 2x_c, 4x_c) + \\ [\text{Max}(L - 2y_c, 0)]^2 + [\text{Max}(B - 2x_c, 0)]^2\end{array}\right)\omega \tag{20}$$

297   Figure 15 compares the H-T failure envelopes derived from PLA and FEA, with the discrepancy

298   generally less than 6%. The contours the equivalent plastic strain at points C and D on Figure

299   15 for given load path of $T/(BH) = 1$ are shown respectively in Figure 16a and b for the one-

300   and two-sided soil failure mechanisms, validating the assumption adopted in Figure 2 for the

301   PLA. Figure 17 presents examples of normalised H-T failure envelopes for foundations with

302   B/L of 0.5. The shape of the failure envelopes is independent of skirt roughness, regardless of

303   the angle of horizontal load. Figure 17 also shows that the effect of foundation embedment is

304   insignificant for the case of $\theta = 0°$, i.e. H parallel to B, but becomes more pronounced for the

305   case of $\theta = 90°$, i.e. H parallel to L, and d/B = 0.2. The normalised H-T failure envelopes are

306   insensitive to the degree of soil strength heterogeneity, as shown in Figure 18. Therefore, the

307   angle of the horizontal load and foundation aspect ratio are the principal influencing factors on

308   the shape of the failure envelopes, as depicted in Figure 19. The shape of the normalised H-T

309   failure envelope can be described by the elliptical expression proposed by Finnie and Morgan

310   (2004)

$$\left(\frac{H}{H_{ult}}\right)^m + \left(\frac{T}{T_{ult}}\right)^n = 1 \tag{21}$$

311   where H_{ult} is the ultimate horizontal capacity in the resultant direction of the horizontal loading,

312   which can be determined from the H_x-H_y failure envelopes using the procedure described in the

313   section 'Translational sliding under combined biaxial horizontal load'. The exponents of m and

314   n are a function of the foundation aspect ratio, B/L and the angle of the horizontal load, θ. The

315   exponents may be expressed as

$$m = 0.71\left(\frac{B}{L}\right)^{0.53\left(1-\frac{4\theta}{\pi}\right)} + \left(\frac{B}{L}\right)^{-0.33\left(1-\frac{4\theta}{\pi}\right)} \tag{22a}$$

$$n = 2.12\tanh\left(0.78\left(\frac{B}{L}\right)^{1.12\left(1-\frac{4\theta}{\pi}\right)} + 0.41\right) \tag{22b}$$

316   Figure 19 shows the normalised H-T failure envelopes for varying angles of horizontal load θ

317   = 0°, 45° and 90°, and for foundations with aspect ratio of B/L = 0.5, 0.75 and 1.0, with

318   predictions using equations (21) and (22). The values of m and n approach 1.75 for square

319   foundations, as proposed by Finnie & Morgan (2004) for circular foundations, irrespective the

320   angle of horizontal loading.

COMPARISON WITH PREVIOUS SOLUTIONS

322   The H-T failure envelopes for a rectangular mudmat with rough skirts derived from the current

323   PLA are compared in Figure 20 with the solutions from Murff et al. (2010) for B/L = 0.5, d/B

324   = 0.1, $s_{u0}/s_{u,avg}$ = 1, $s_{u,avg}/\gamma'd$ = 1.67 ($\gamma'd/s_{u0}$ = 0.6) and loading angles of 45 and 67.5°.

325   Comparisons with solutions from Nouri et al. (2014) were made for rectangular and square

326   mudmats with very shallow skirts and angles of horizontal loading of θ = 0° or 90°. Close

327   agreement with the previous solutions presented is achieved for the intact contact condition,

328   where no gap occurs adjacent to the 'active' regions of the skirt. Figure 20 also shows the H-T

329   interaction diagram including loss of contact due to the presence of a gap. The capacity is

330   reduced by approximately 17% for pure horizontal loading and 22% for pure torsional loading

331 compared with the case for no gap presented in Murff et al. (2010). Significant reduction in

332 horizontal and torsional was also evident due to the presence of the gap for the cases

333 investigated by Nouri et al. (2014). The failure envelopes predicted from equations (21) and

334 (22) are plotted in Figure 20 together with the PLA results, confirming the accuracy of the

335 proposed expressions in determining the failure envelopes for cases of arbitrary angles of the

336 resultant horizontal load.

CONCLUSIONS

338 The response of skirted rectangular foundations to biaxial horizontal loading and combined

339 horizontal-torsional loading was investigated by plasticity limit analyses and the results were

340 compared with finite element analyses. An approach, based on the interactions between the

341 base shearing and skirt bearing failure, is proposed to determine the ultimate translational

342 resistance under biaxial horizontal load. For combined H-T loading, a general expression is

343 presented for predicting the normalised failure envelopes. The shape of the normalised H-T

344 failure envelope is affected by foundation aspect ratio and angle of horizontal loading, but

345 insensitive to skirt roughness and soil strength heterogeneity. The effect of foundation

346 embedment becomes significant when the horizontal load is applied parallel to the long edge of

347 rectangular foundations.

348 The proposed procedure for determining the failure envelopes enable an automated design tool

349 to assess the translational and torsional sliding of mudmats.

ACKNOWLEDGEMENTS

362 **NOTATTION**

A	bearing area of mudmat
B	width of mudmat
d	skirt depth
H_x	horizontal load along the x-axis
H_{xult}	ultimate horizontal capacity along the x-axis
H_y	horizontal load along the y-axis
H_{yult}	ultimate horizontal capacity along the y-axis
k	shear strength gradient
L	length of mudmat
m, n	exponents for the general ellipse for the normalised H-T failure envelopes
N_{px}	skirt bearing capacity factor in x-direction
N_{py}	skirt bearing capacity factor in y-direction
s_u	undrained shear strength of soil
$s_{u,avg}$	average undrained shear strength of soil over the depth of the skirts
s_{u0}	undrained shear strength of soil at skirt tip level
T	torsion
T_{ult}	ultimate torisonal capacity
$W_{\gamma H}$	work done by the self-weight of soil for translational sliding
$W_{\gamma T}$	work done by the self-weight of soil for torsional sliding
x_c	x-coordinate of the rotation centre in the upper bound mechanisms
y_c	y-coordinate of the rotation centre in the upper bound mechanisms
α_{skirt}	skirt friction ratio
$\beta_1, \beta_2, \beta_3, \beta_4$	slope angles of the soil wedges in the upper bound mechanisms
γ'	effective unit weight of the soil
δ	number of sides to upper bound mechanism
ΔH_x	additional capacity along the x-axis
ΔH_y	additional capacity along the y-axis
ΔH_{xult}	ultimate additional capacity along the x-axis
ΔH_{yult}	ultimate additional capacity along the y-axis
ΔW	plastic work at discontinuities and deforming regions
θ	angle of resultant horizontal load from the x-axis
θ'	angle of resultant additional horizontal capacity from the x-axis
θ_u	direction of motion for translational sliding
ξ	a parameter for the interaction between ΔH_x and ΔH_y.

363

364 **APPENDIX A DERIVATION OF THE WORK DONE BY SELF-WEIGHT OF SOIL**

365 **WEDGES UNDER COMBINED H-T LOADING**

366 The derivation of the work done by the self-weight of the soil wedge W_1 shown in Figure 2 is

367 demonstrated as below.

368 The self-weight of the slice of soil shown in Figure 1b is

369 $\Delta w = \gamma' \Delta V = \gamma' \frac{1}{2} d^2 \cot\beta_1 \cdot dy$ A.1

370   where ΔV is the volume of the slice of the soil.

371   The magnitude of the vertical displacement is

372    $u_z = u_x \tan\beta_1 = \omega(y_c - y)\tan\beta_1$ A.2

373   If the centre of rotation falls within the foundation footprint, the integration limit is (-L/2, y_c).

374   Otherwise, the soil wedge W_1 runs along the entire length of long edge of the foundation and

375   the integration limit becomes (-L/2, L/2).

376   Therefore, the work done by self-weight of soil wedge W_1 is integrated as

377

$$\Delta W_{\gamma T\_1} = (\delta - 2)\int_{-L/2}^{Min(y_c,L/2)} u_z \cdot \Delta w = (\delta - 2)\int_{-L/2}^{Min(y_c,L/2)} \omega(y_c - y)\tan\beta_1 \times \frac{\gamma' d^2}{2}\cot\beta_1 \cdot dy$$

$$= -\frac{(\delta - 2)\gamma' d^2}{2}\omega \cdot \frac{1}{2}(y - y_c)^2\Big|_{-L/2}^{\min(y_c,L/2)} = \frac{(\delta - 2)\gamma' d^2}{16}Min(L + 2y_c, 2L)Max(L + 2y_c, 4y_c)\omega$$

        A.3

378   The work done by the self-weight of the soil wedges of W_2, W_3 and W_4 can be calculated in the

379   same manner as W_1. Equation (16) is then obtained by summing them together.

380   **REFERENCES**

381   Acosta-Martinez, H. E., Gourvenec, S. M. & Randolph, M. F. (2010) Effect of gapping on the
382   transient and sustained uplift capacity of a shallow skirted foundation in clay. *Soils and*
383   *Foundations* **50(5)**:725-735, http://doi.org/10.3208/sandf.50.725.

384   API (2011) *Recommended Practice 2GEO Geotechnical and Foundation Design*
385   *Considerations - 1st Edition.* American Petroleum Institute, Washington.

386   Bransby, M. F. & Randolph, M. F. (1999) The effect of embedment depth on the undrained
387   response of skirted foundations to combined loading. *Soils and Foundations* **39(4)**:19-
388   33, http://doi.org/10.3208/sandf.39.4_19.

389   Britto, A. M. & Kusakabe, O. (1982) Stability of unsupported axisymmetric excavations in soft
390   clay. *Géotechnique* **32(3)**:261-270, http://dx.doi.org/10.1680/geot.1982.32.3.261.

391   Feng, X., Randolph, M. F., Gourvenec, S. & Wallerand, R. (2014) Design approach for
392   rectangular mudmats under fully three-dimensional loading. *Géotechnique* **64(1)**:51-63,
393   http://dx.doi.org/10.1680/geot.13.P.051.

394   Finnie, I. M. S. & Morgan, N. (2004) Torsional loading of subsea structures In *the 14th Int.*

395 *Offshore and Polar Eng. Conf.* International Society of Offshore and Polar Engineers
396 (ISOPE), Toulon, France, pp. 326-333.

397 ISO (2003) ISO19901-4: *Petroleum and natural gas industries specific requirements for*
398 *Offshore Structures - Part 4: Geotechnical and foundation design considerations - 1st*
399 *Edition.* International Standards Organisation, Geneva.

400 Mana, D. S. K., Gourvenec, S. & Randolph, M. F. (2013) Experimental investigation of reverse
401 end bearing of offshore shallow foundations. *Canadian Geotechnical Journal*
402 **50(10)**:1022-1033, http://dx.doi.org/10.1139/cgj-2012-0428.

403 Martin, C.M. (2011) The use of adaptive finite-element limit analysis to reveal slip-line fields.
404 *Géotechnique Letters* **1**:23-29, http://dx.doi.org/10.1680/geolett.11.00018.

405 Murff, J. D., Aubeny, C. P. & Yang, M. (2010) The effect of torsion on the sliding resistance
406 of rectangular foundations In *the 2nd Int. Symp. on Front. in Offshore Geotech. (ISFOG*
407 *2010)*, Perth, Australia, pp. 439-443.

408 Nouri, H., Biscontin, G. & Aubeny, C. (2014) Undrained sliding resistance of shallow
409 foundations subject to torsion. *Journal of Geotechnical and Geoenvironmental*
410 *Engineering* **140(8)**:04014042, http://dx.doi.org/10.1061/(ASCE)GT.1943-
411 5606.0001138.

412

413

414   Table 1 Plastic work for combined H_x-H_y loading
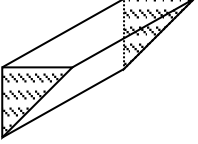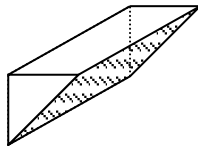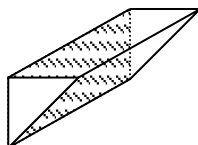
Discontinuities	Plastic work
Foundation base	$\Delta W_b = uAs_{u0}$
Ends of soil wedges 	$\Delta W_e = \dfrac{\delta ud^2}{3}\left(\dfrac{\cos\theta_u}{\sin\beta_1}+\dfrac{\sin\theta_u}{\sin\beta_2}\right)\left(\dfrac{4s_{u,avg}}{s_{u0}}-1\right)s_{u0}$
Slopes of the wedges 	$\Delta W_s = 2\delta ud\left(\dfrac{L\cos\theta_u}{\sin2\beta_1}+\dfrac{B\sin\theta_u}{\sin2\beta_2}\right)s_{u,avg}$
Skirt walls 	$\Delta W_w = \delta u\alpha_{skirt}d\left(L\sqrt{(\cos\theta_u\tan\beta_1)^2+\sin^2\theta_u}+B\sqrt{(\sin\theta_u\tan\beta_2)^2+\cos^2\theta_u}\right)s_{u,avg}$

415

416   Table 2   Optimised solutions of the wedge angle for calculating the skirt bearing capacity

417   factor
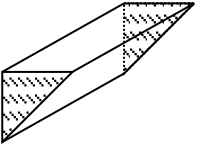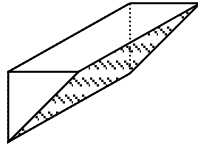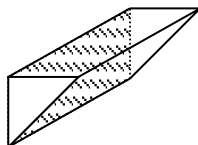
Soil profile	Skirt roughness	Embedment ratio	B/L = 0.5		B/L = 1.0
			x-axis	y-axis	x- and y- axis
$s_{u,avg}/s_{u0} = 1$;	$\alpha_{skirt} = 0$	d/B = 0.05	β = 45.25°	β = 45.49°	β = 45.49°
		d/B = 0.10	β = 45.49°	β = 45.96°	β = 45.96°
		d/B = 0.20	β = 45.96°	β = 46.84°	β = 46.84°
$s_{u,avg}/s_{u0} = 0.5$;	$\alpha_{skirt} = 1$	d/B = 0.05	β = 35.45°	β = 35.63°	β = 35.63°
		d/B = 0.10	β = 35.63°	β = 35.98°	β = 35.98°
		d/B = 0.20	β = 35.98°	β = 36.65°	β = 36.65°

418
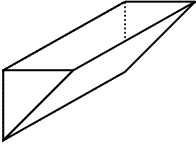
419   Table 3   Steps for determining the H_x-H_y failure envelopes for embedded rectangular

420   mudmats

421

Step	Mudmats with smooth skrits	Mudmats with rough skrits
1	Assume a direction of foundation sliding θ_u and calculate the x- and y- component of the basal sliding resistance by $As_{u0}\cos\theta_u$ and $As_{u0}\sin\theta_u$, respectively.	
2	Calculate the ultimate additional capacity provided by the skirts $\Delta H_{xult} = N_{px}dLs_{u0}$ and $\Delta H_{yult} = N_{py}dBs_{u0}$ according to equation (3)	

3	The additional capacity is independent of the direction of foundation sliding. Hence, $\Delta H_x = \Delta H_{xult}$ and $\Delta H_y = \Delta H_{yult}$	Determine the value of θ' for given θ_u using equation (14). Substitute $\Delta H_y / \Delta H_x = \tan \theta'$ into equation (12) and solve the unknowns ΔH_x and ΔH_y.
4	Calculate the failure loads H_x and H_y on the failure envelopes for the embedded foundations for given direction of sliding θ_u using equation (9). The load angle of θ is then calculated as $\theta = \tan^{-1}(H_y/H_x)$.	
5	Vary the value of θ_u and repeat steps 1 to 4 to constitute the whole H_x-H_y failure envelopes.	

422

423

424   Table 4 Plastic work for combined H-T loading (Figure 2)

Discontinuities and deforming regions	Plastic work
Foundation base	$\Delta W_b = \omega s_{u0} \int_{-B/2}^{B/2} \int_{-L/2}^{L/2} \sqrt{(x-x_c)^2 + (y-y_c)^2} \, dxdy$
Ends of soil wedges	$\Delta W_{e1} = \dfrac{1}{12} \dfrac{\omega d^2 [4y_c + \delta Max(L - 2y_c, 0)]}{\sin\beta_1} \left(\dfrac{4s_{u,avg}}{s_{u0}} - 1 \right) s_{u0}$
	$\Delta W_{e2} = \dfrac{1}{12} \dfrac{\omega d^2 [-4x_c + \delta Max(B + 2x_c, 0)]}{\sin\beta_2} \left(\dfrac{4s_{u,avg}}{s_{u0}} - 1 \right) s_{u0}$
	$\Delta W_{e3} = \dfrac{1}{12} \dfrac{\omega d^2 [4(\delta-1)y_c + \delta Max(L - 2y_c, 0)]}{\sin\beta_3} \left(\dfrac{4s_{u,avg}}{s_{u0}} - 1 \right) s_{u0}$
	$\Delta W_{e4} = \dfrac{1}{12} \dfrac{\omega d^2 [-4(\delta-1)x_c + \delta Max(B + 2x_c, 0)]}{\sin\beta_4} \left(\dfrac{4s_{u,avg}}{s_{u0}} - 1 \right) s_{u0}$
Slopes of the wedges	$\Delta W_{s1} = \dfrac{1}{4} \dfrac{\omega d [Max(L + 2y_c, 4y_c)Min(L + 2y_c, 2L) + (\delta-1)(L - 2y_c)Max(L - 2y_c, 0)]}{\sin 2\beta_1} s_{u,avg}$
	$\Delta W_{s2} = \dfrac{1}{4} \dfrac{\omega d [Max(B - 2x_c, -4x_c)Min(2B, B - 2x_c) + (\delta-1)(B + 2x_c)Max(B + 2x_c, 0)]}{\sin 2\beta_2} s_{u,avg}$
	$\Delta W_{s3} = \dfrac{1}{4} \dfrac{\omega d [(L - 2y_c)Max(L - 2y_c, 0) + (\delta-1)Max(L + 2y_c, 4y_c)Min(L + 2y_c, 2L)]}{\sin 2\beta_3} s_{u,avg}$
	$\Delta W_{s4} = \dfrac{1}{4} \dfrac{\omega d [(B + 2x_c)Max(B + 2x_c, 0) + (\delta-1)Max(B - 2x_c, -4x_c)Min(B - 2x_c, 2B)]}{\sin 2\beta_4} s_{u,avg}$
Skirt walls Note: For	$\Delta W_{w1} = \dfrac{\omega d \alpha_{skirt} s_{u,avg}}{2 \tan\beta_1} \left[Y_2 \sqrt{Y_2^2 + Z^2} - Y_1 \sqrt{Y_1^2 + Z^2} + Z^2 \ln\left(\left(\sqrt{Y_2^2 + Z^2} + Y_2\right) / \left(\sqrt{Y_1^2 + Z^2} + Y_1\right) \right) \right]$ where $Y_1 = (-L/2 - y_c)\tan\beta_1$; $Y_2 = [(\delta-1)(L/2 - y_c) + (2-\delta)\min(L/2 - y_c, 0)]$; $Z = B/2 - x_c$
	$\Delta W_{w2} = \dfrac{\omega d \alpha_{skirt} s_{u,avg}}{2 \tan\beta_2} \left[Y_2 \sqrt{Y_2^2 + Z^2} - Y_1 \sqrt{Y_1^2 + Z^2} + Z^2 \ln\left(\left(\sqrt{Y_2^2 + Z^2} + Y_2\right) / \left(\sqrt{Y_1^2 + Z^2} + Y_1\right) \right) \right]$ where $Y_1 = [(\delta-1)(-B/2 - x_c) + (2-\delta)Max(-B/2 - x_c, 0)]\tan\beta_2$; $Y_2 = (B/2 - x_c)\tan\beta_2$; $Z = L/2 + y_c$
	$\Delta W_{w3} = \dfrac{\omega d \alpha_{skirt} s_{u,avg}}{2 \tan\beta_3} \left[Y_2 \sqrt{Y_2^2 + Z^2} - Y_1 \sqrt{Y_1^2 + Z^2} + Z^2 \ln\left(\left(\sqrt{Y_2^2 + Z^2} + Y_2\right) / \left(\sqrt{Y_1^2 + Z^2} + Y_1\right) \right) \right]$ where $Y_1 = [(\delta-1)(-L/2 - y_c) + (2-\delta)Min(L/2 - y_c, 0)]\tan\beta_3$; $Y_2 = (L/2 - y_c)\tan\beta_3$; $Z = B/2 + x_c$

comparison with FEA, $\delta = 1$ is presumed only for $\alpha_{skirt} = 0$ in PLA.	$\Delta W_{w4} = \dfrac{\omega d \alpha_{skirt} s_{u,avg}}{2 \tan \beta_4} \left[Y_2 \sqrt{Y_2^2 + Z^2} - Y_1 \sqrt{Y_1^2 + Z^2} + Z^2 \ln\left(\left(\sqrt{Y_2^2 + Z^2} + Y_2\right) \middle/ \left(\sqrt{Y_1^2 + Z^2} + Y_1\right)\right) \right]$ where $Y_1 = (-B/2 - x_c)\tan\beta_4$; $Y_2 = \left[(\delta - 1)(B/2 - x_c) + (2 - \delta)\text{Max}(-B/2 - x_c, 0)\right]\tan\beta_4$; $Z = L/2 + y_c$
Deforming regions	$\Delta W_{v1} = \dfrac{1}{12} \dfrac{\omega d^2 \left[\delta L + (2 - \delta)\text{Min}(L, 2y_c)\right]}{\sin\beta_1} \left(\dfrac{4s_{u,avg}}{s_{u0}} - 1\right) s_{u0}$
	$\Delta W_{v2} = \dfrac{1}{12} \dfrac{\omega d^2 \left[\delta B + (2 - \delta)\text{Min}(B, -2x_c)\right]}{\sin\beta_2} \left(\dfrac{4s_{u,avg}}{s_{u0}} - 1\right) s_{u0}$
	$\Delta W_{v3} = \dfrac{1}{12} \dfrac{\omega d^2 \left[\delta L - (2 - \delta)\text{Min}(L, 2y_c)\right]}{\sin\beta_3} \left(\dfrac{4s_{u,avg}}{s_{u0}} - 1\right) s_{u0}$
	$\Delta W_{v4} = \dfrac{1}{12} \dfrac{\omega d^2 \left[\delta B - (2 - \delta)\text{Min}(B, -2x_c)\right]}{\sin\beta_4} \left(\dfrac{4s_{u,avg}}{s_{u0}} - 1\right) s_{u0}$

425

426

427 **FIGURE CAPTIONS**

428 Figure 1 Failure mechanism under biaxial horizontal load

429 Figure 2 Failure mechanisms under combined horizontal-torsional load

430 Figure 3 FE mesh for rectangular mudmats d/B = 0.1, B/L = 0.5

431 Figure 4 Pure horizontal sliding resistance

432 Figure 5 Pure torsional sliding resistance

433 Figure 6 Comparison of H_x-H_y failure envelopes obtained from PLA and FEA (B/L = 0.5)

434 Figure 7 Soil failure mechanisms obtained from FEA for biaxial horizontal loads

435 Figure 8 Interaction diagram for the biaxial horizontal loads

436 Figure 9 Interaction between the two components of the additional skirt bearing capacity
437 (B/L = 0.5)

438 Figure 10 Normalised ΔH_x-ΔH_y failure envelopes for foundations with rough skirts

439 Figure 11 Zones and the point of transition defining the H_x-H_y failure envelopes

440 Figure 12 Interaction between the angle of foundation motion (θ_u) and loading angle (θ')

441 Figure 13 Prediction of the normalised H_x-H_y failure envelopes for mudmats with rough
442 skirts

443 Figure 14 Prediction of the normalised H_x-H_y failure envelopes for mudmats with smooth
444 skirts

445 Figure 15 Comparison of H-T failure envelopes obtained from PLA and FEA (B/L = 0.5)

446 Figure 16 Soil failure mechanisms obtained from FEA for horizontal and torsional load

447 Figure 17 Effect of skirt roughness and foundation embedment on normalised H-T failure
448 envelopes

449 Figure 18 Effect of soil shear strength profile on normalised H-T failure envelopes ($\theta = 90°$)

450 Figure 19 Effect of foundation geometry and direction of horizontal loading on normalised
451 H-T failure envelopes

452 Figure 20 Comparisons between current PLA and proposed expressions with previous
453 solutions

454

455

456

457

a) Plane view

b) Elevation view of section I-I

c) Passive soil wedge W_1
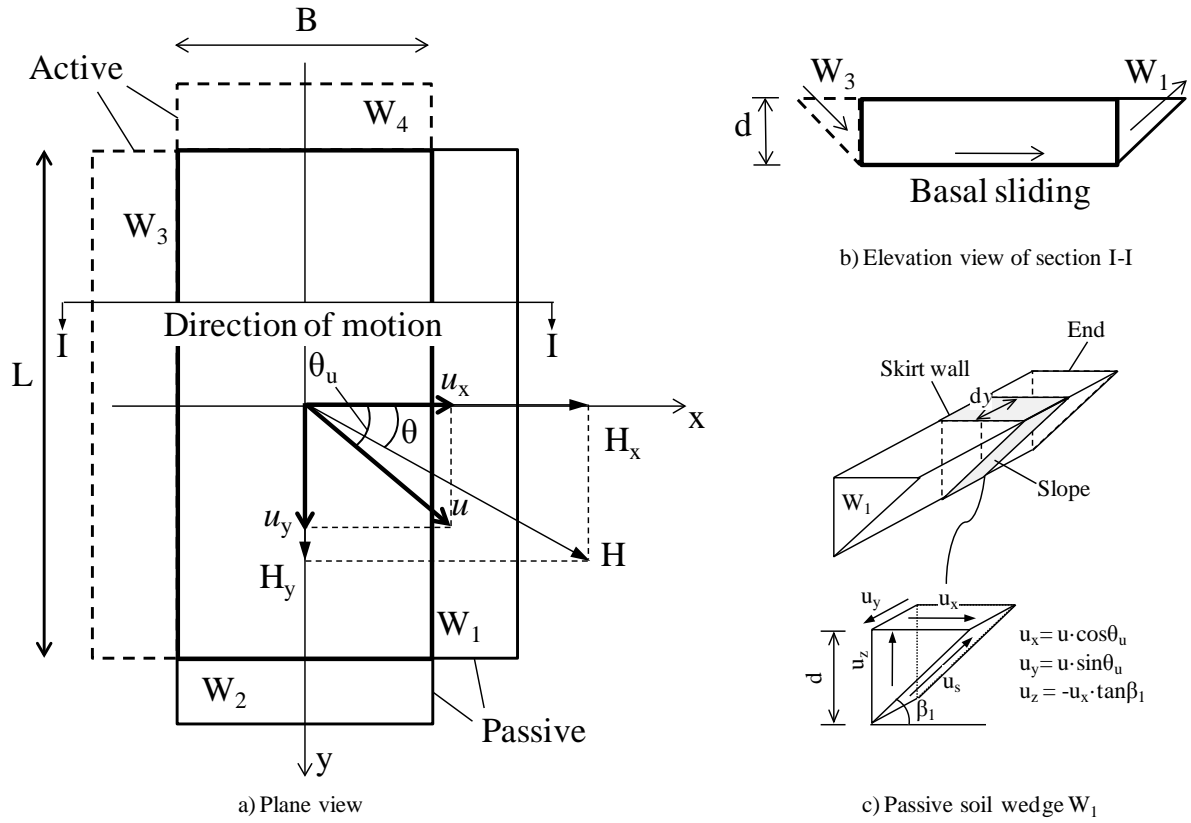
458

459 Figure 1 Failure mechanism under biaxial horizontal load
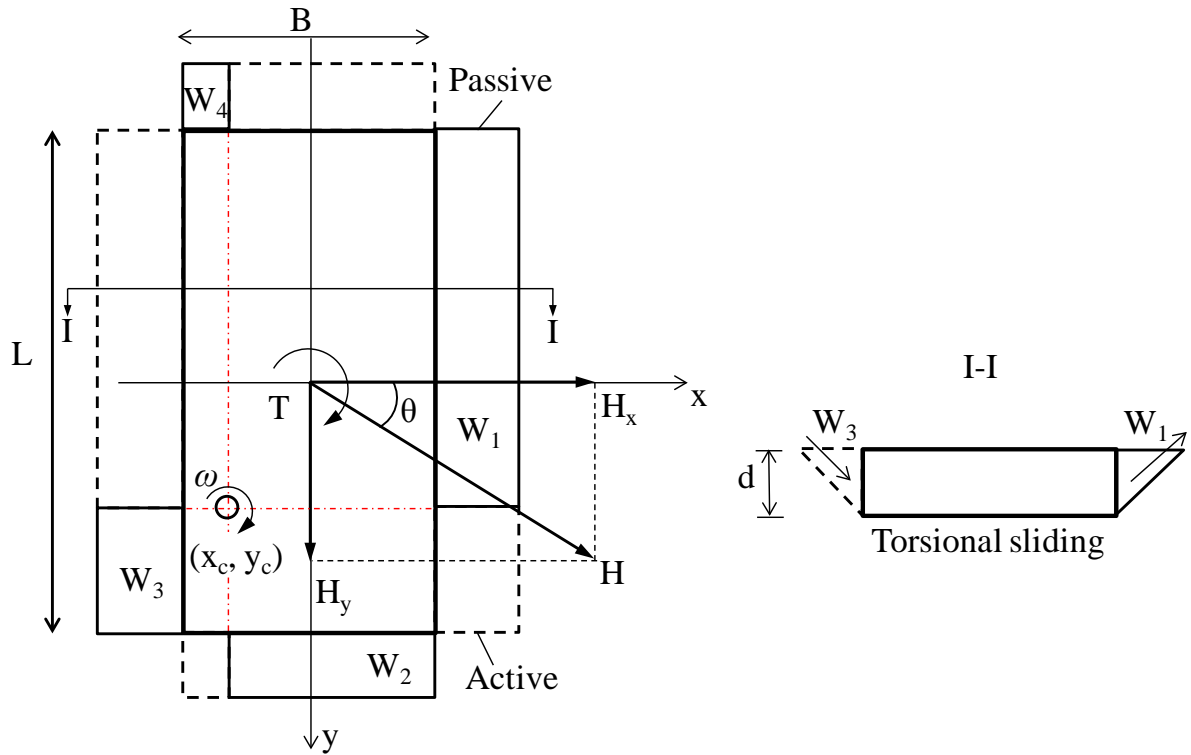
460

461 Figure 2 Failure mechanisms under combined horizontal-torsional load

462

463   Figure 3 FE mesh for rectangular mudmats d/B = 0.1, B/L = 0.5

464
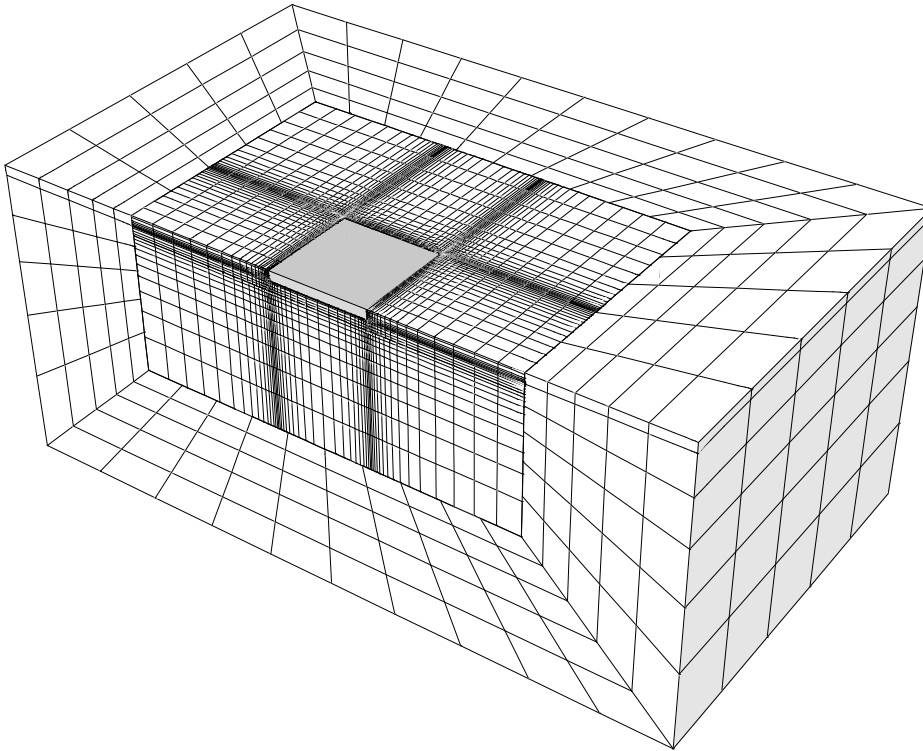
465
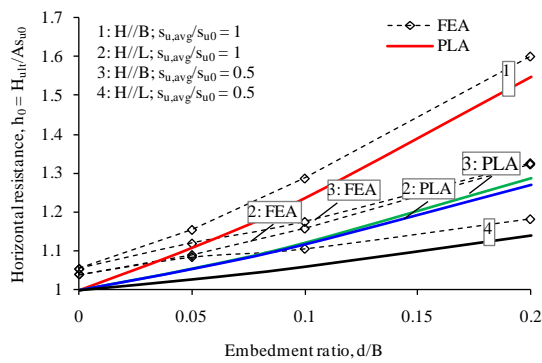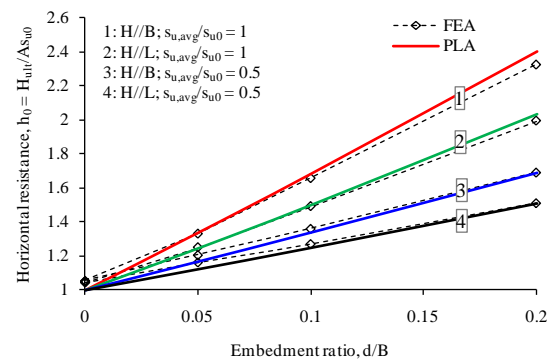
a) S: allowing gap   b) R: no gap

466   Figure 4 Pure horizontal sliding resistance

467
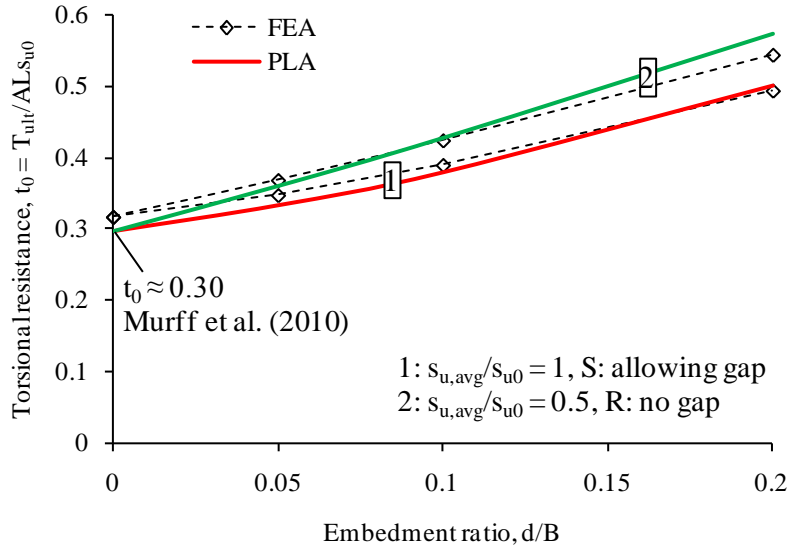
Figure 5 Pure torsional sliding resistance
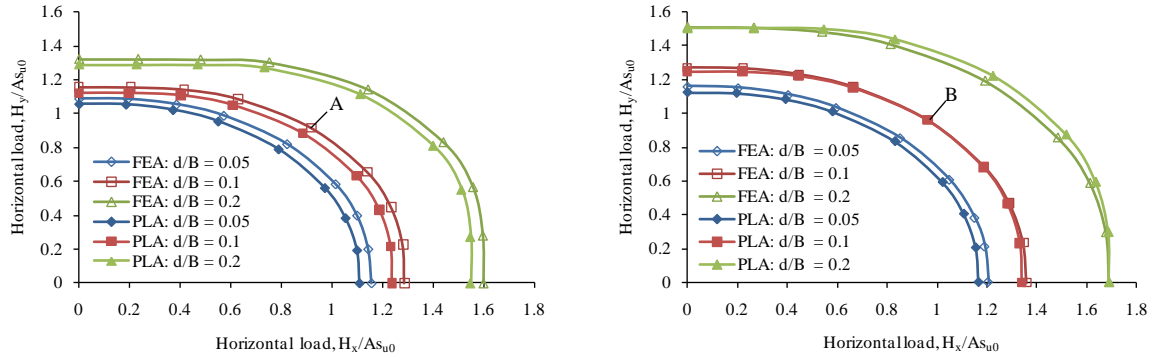
a) $s_{u,avg}/s_{u0} = 1$, S: allowing gap

b) $s_{u,avg}/s_{u0} = 0.5$, R: no gap

469   Figure 6 Comparison of H_x-H_y failure envelopes obtained from PLA and FEA (B/L = 0.5)
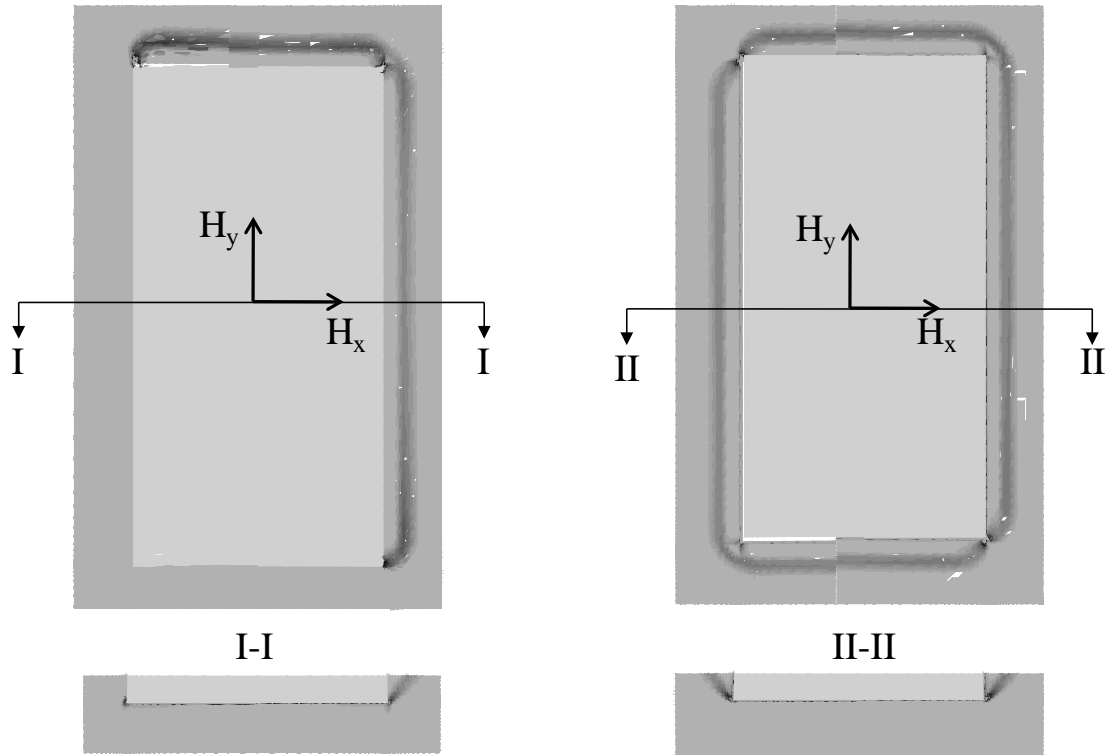
a) One-sided, $H_y/H_x = 1$ ($\theta = 45°$)

b) Two-sided, $H_y/H_x = 1$ ($\theta = 45°$)

470   Figure 7 Soil failure mechanisms obtained from FEA for biaxial horizontal loads

471
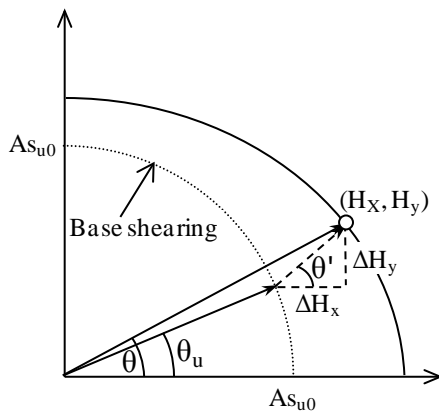
472   Figure 8 Interaction diagram for the biaxial horizontal loads
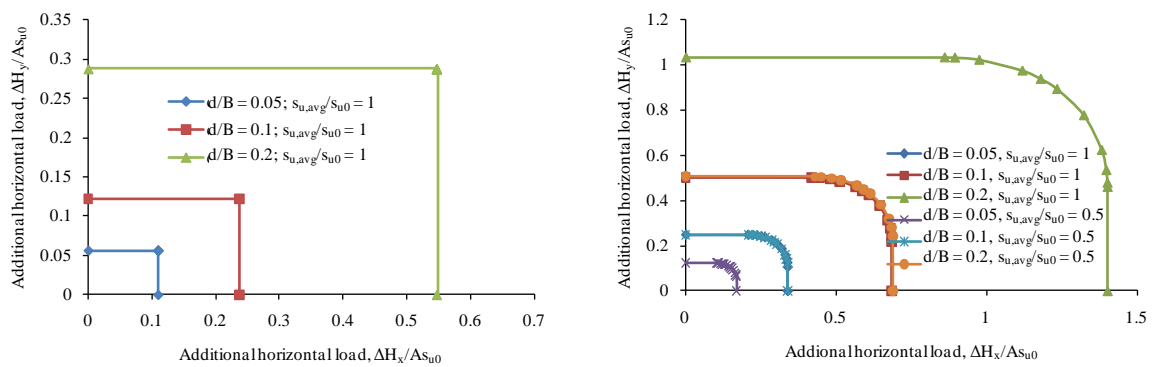
a) $s_{u,avg}/s_{u0} = 1$, S: allowing gap

b) $s_{u,avg}/s_{u0} = 0.5$, R: no gap

473   Figure 9 Interaction between the two components of the additional skirt bearing capacity
474   (B/L = 0.5)

475
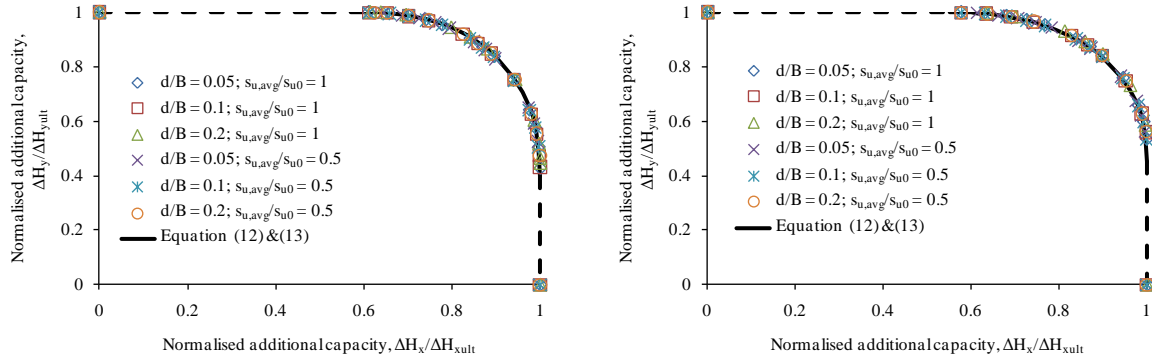
a) B/L = 0.5

b) B/L = 0.75
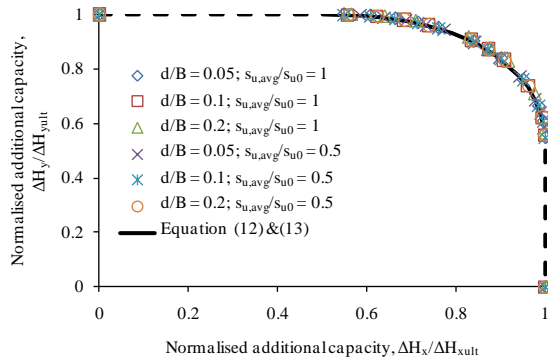
c) B/L = 1

476   Figure 10 Normalised ΔH_x-ΔH_y failure envelopes for foundations with rough skirts
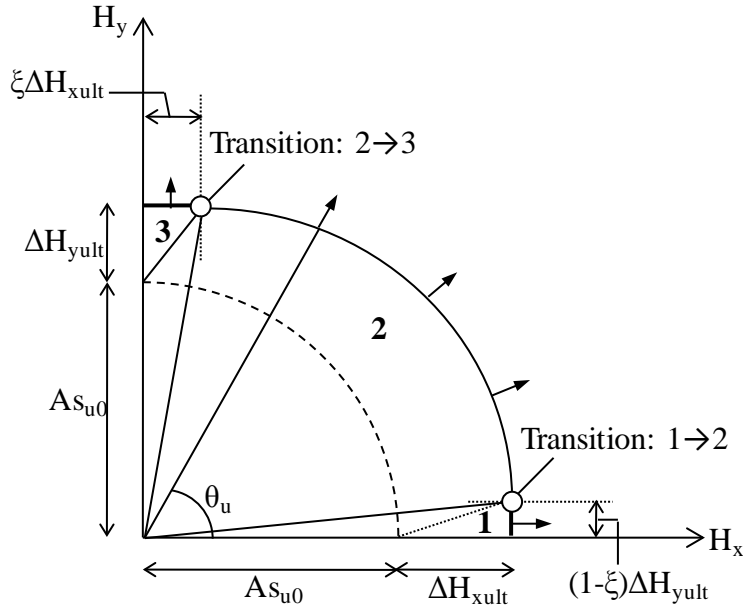
Zone 1: slide along x-axis
Zone 2: slide in the direction of θ_u
Zone 3: slide along y-axis

477

478   Figure 11 Zones and the point of transition defining the H_x-H_y failure envelopes

479
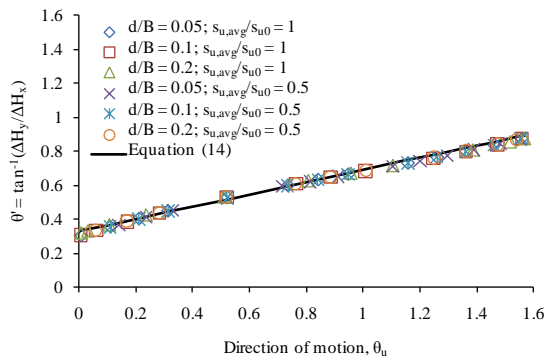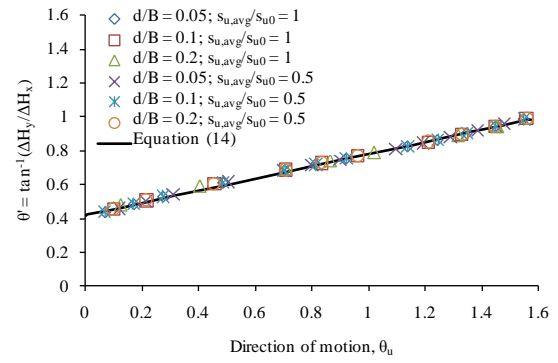
a) B/L = 0.5   b) B/L = 0.75
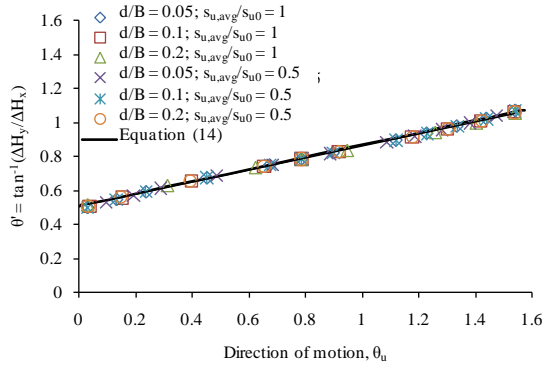
c) B/L = 1

480   Figure 12 Interaction between the angle of foundation motion (θ_u) and loading angle (θ')
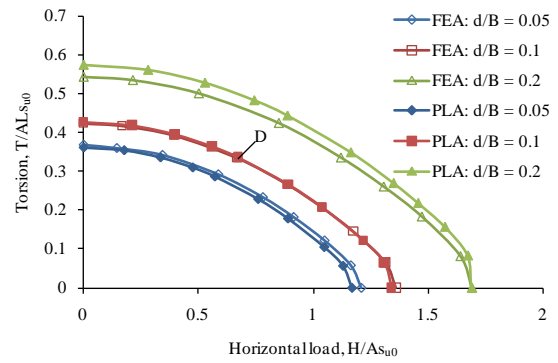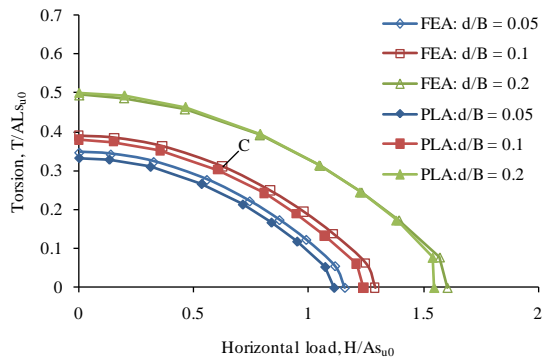
a) $s_{u,avg}/s_{u0} = 1$, $\theta = 0°$, S: allowing gap

b) $s_{u,avg}/s_{u0} = 0.5$, $\theta = 0°$, R: no gap
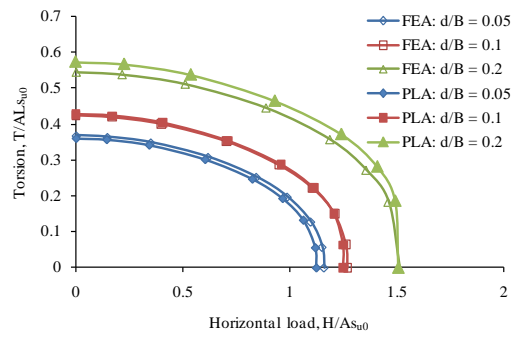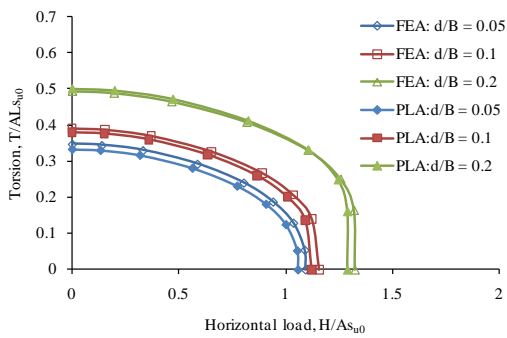
c) $s_{u,avg}/s_{u0} = 1$, $\theta = 90°$, S: allowing gap

d) $s_{u,avg}/s_{u0} = 0.5$, $\theta = 90°$, R: no gap

481   Figure 13 Comparison of H-T failure envelopes obtained from PLA and FEA (B/L = 0.5)
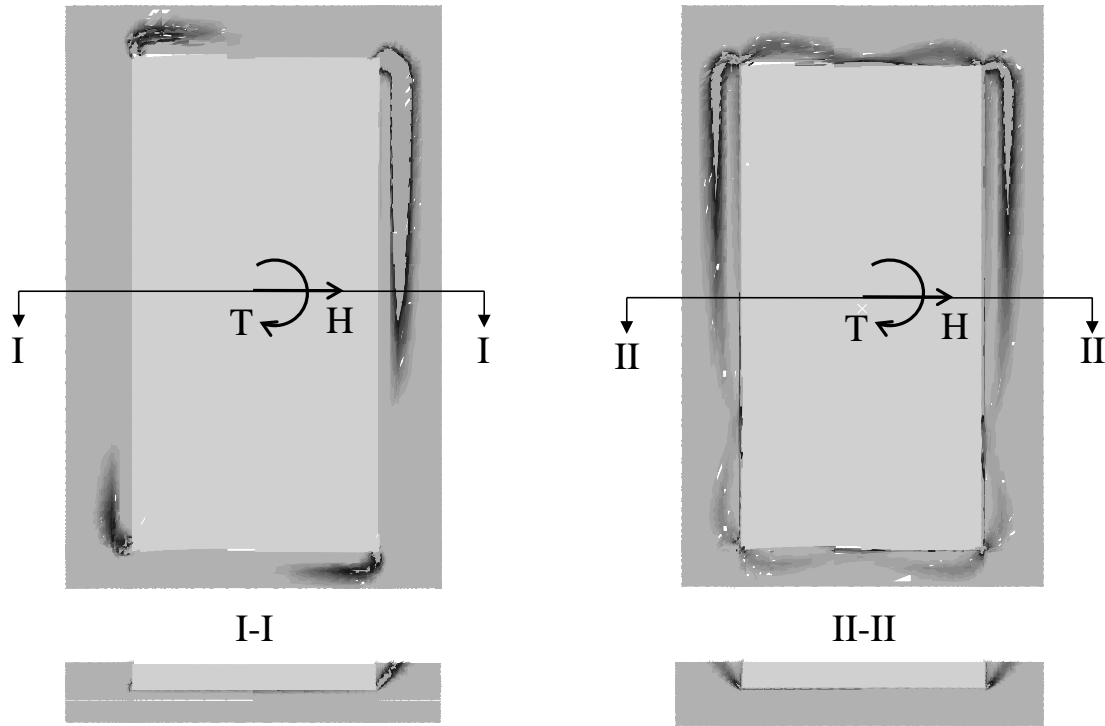
a) One-sided, T/(BH) = 1 (θ = 0°) b) Two-sided, T/(BH) = 1 (θ = 0°)

482 Figure 14 Soil failure mechanisms obtained from FEA for horizontal and torsional load
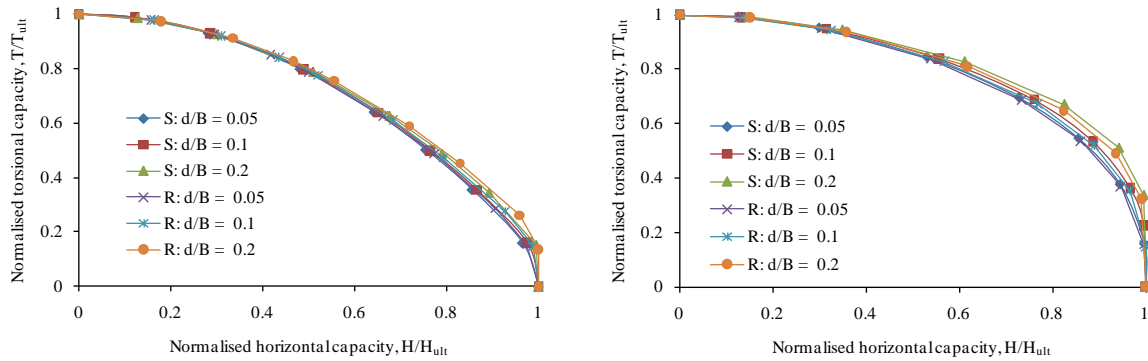
a) $s_{u,avg}/s_{u0} = 1$, θ = 0° b) $s_{u,avg}/s_{u0} = 0.5$, θ = 90°

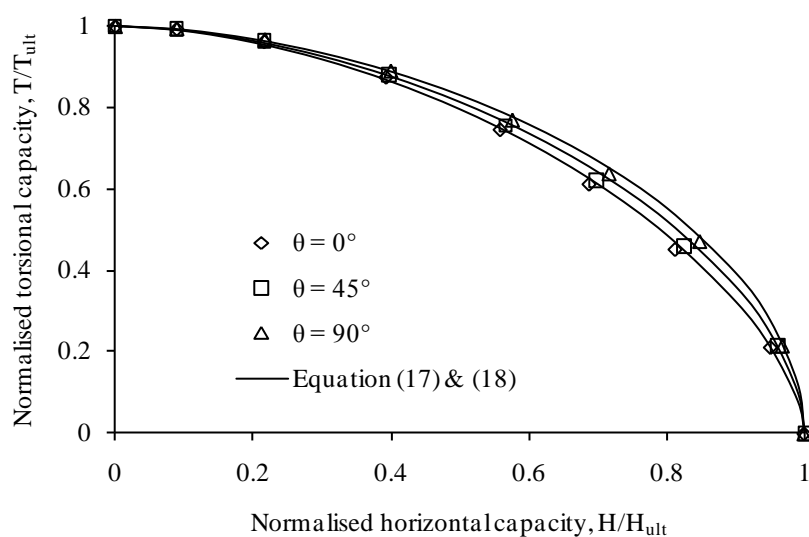483 Figure 15 Effect of skirt roughness and foundation embedment on normalised H-T failure
484 envelopes
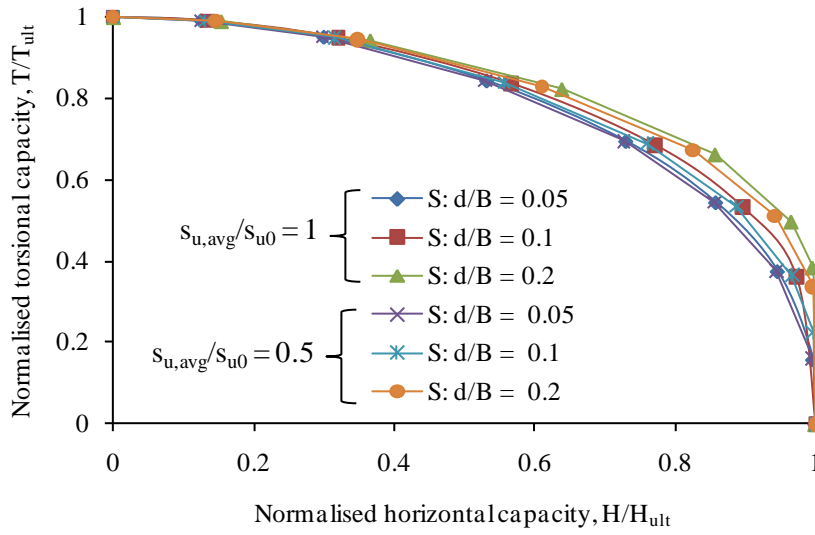
485

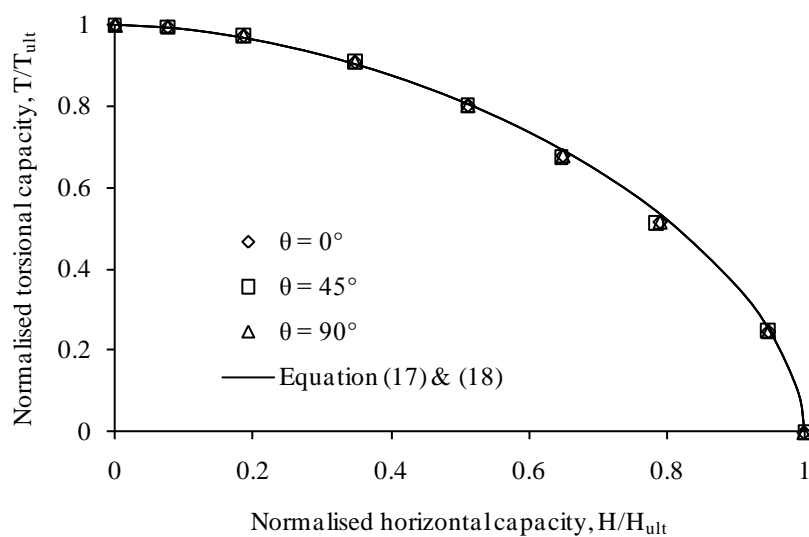486   Figure 16 Effect of soil shear strength profile on normalised H-T failure envelopes ($\theta = 90°$)
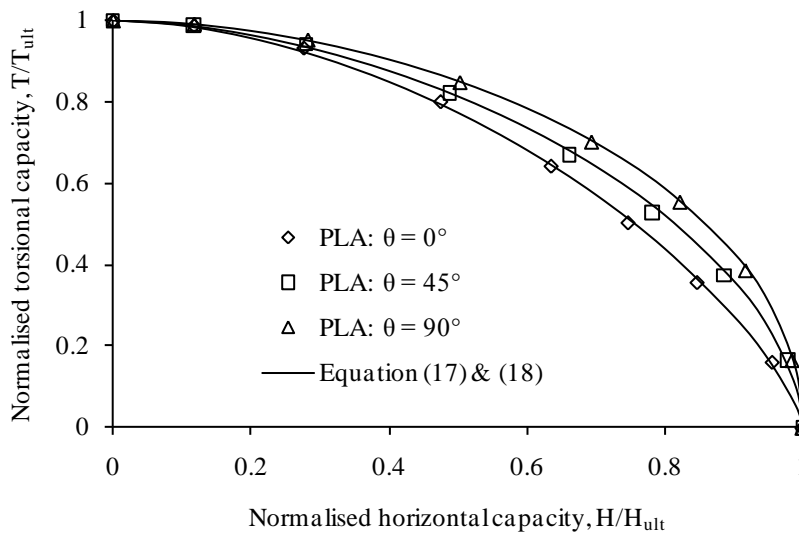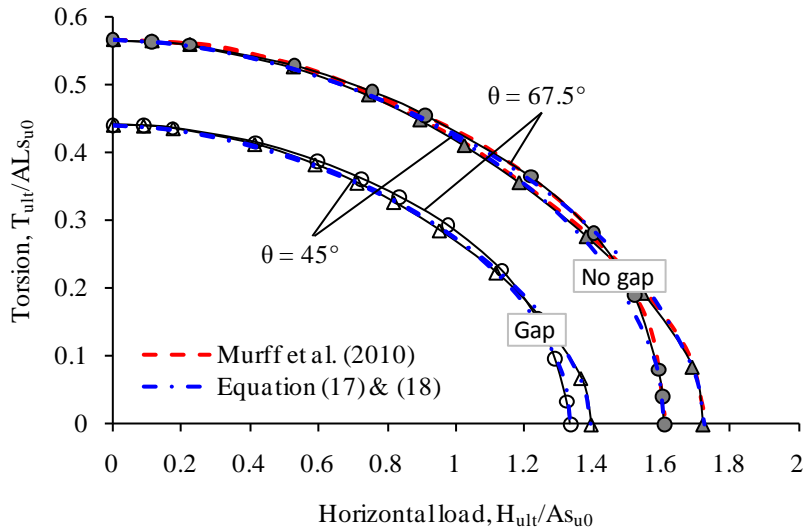

487

488   a) B/L = 0.5

489

490 b) B/L = 0.75
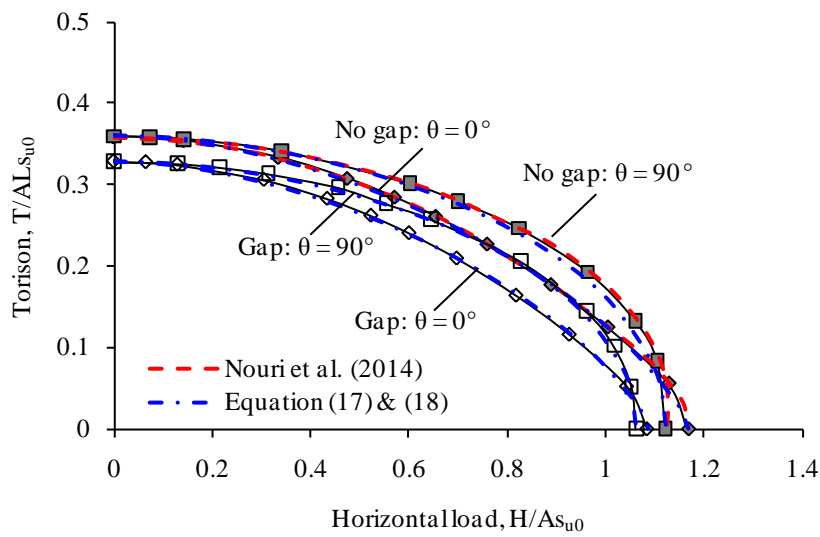

491

492 c) B/L = 1

493 Figure 17 Effect of foundation geometry and direction of horizontal loading on normalised H-
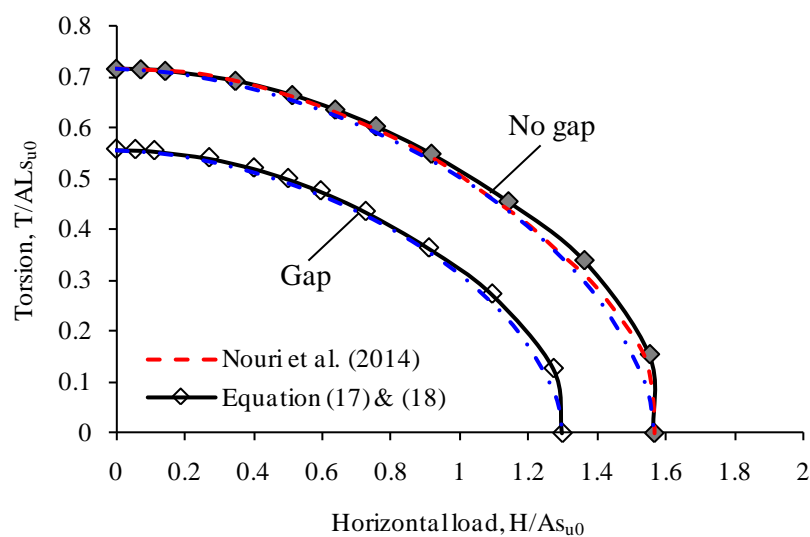
494 T failure envelopes

495

496

497   a) Comparison with Murff et al. (2010): B/L = 0.5; d/B = 0.1

498

499   b) Comparison with Nouri et al. (2014): B/L = 0.5; d/B = 0.025(B/d = 40)

500

501

502   c) Comparison with Nouri et al. (2014): B/L = 1; d/B = 0.071(B/d = 14)

503   Figure 18   Comparisons between current PLA and proposed expressions with previous
504   solutions

505